REPORT DOCUMENTATION PAGE

AFRL-SR-BL-TR-01-

$O642$

1. AGENCY USE ONLY *(Leave blank)*	2. REPORT DATE	3. REPORT TYPE AND DATES COVERED
		01 Apr 98 to 31 Mar 01 Final

4. TITLE AND SUBTITLE
Programmable Mesooptics with Resonant Near-Field Nonlinear Nanostructures

5. FUNDING NUMBERS
61102F
2305/DX

6. AUTHOR(S)
Dr. Fainman

7. PERFORMING ORGANIZATION NAME(S) AND ADDRESS(ES)
University of California San Diego
9500 Gilman Dr
LaJolla, CA 92093

8. PERFORMING ORGANIZATION REPORT NUMBER

9. SPONSORING/MONITORING AGENCY NAME(S) AND ADDRESS(ES)
AFOSR/NE
801 North Randolph Street Rm 732
Arlington, VA 22203-1977

10. SPONSORING/MONITORING AGENCY REPORT NUMBER

F49620-98-1-0427

11. SUPPLEMENTARY NOTES

12a. DISTRIBUTION AVAILABILITY STATEMENT
APPROVAL FOR PUBLIC RELEASED; DISTRIBUTION UNLIMITED

12b. DISTRIBUTION CODE

13. ABSTRACT *(Maximum 200 words)*

The goal of this project is to conduct basic research towards the development of mesooptics diffractive optical elements (DOE) with programmability for application to optoelectronic and photonic systems.

20020107 062

14. SUBJECT TERMS

15. NUMBER OF PAGES

16. PRICE CODE

17. SECURITY CLASSIFICATION OF REPORT	18. SECURITY CLASSIFICATION OF THIS PAGE	19. SECURITY CLASSIFICATION OF ABSTRACT	20. LIMITATION OF ABSTRACT
UNCLASSIFIED	UNCLASSIFIED	UNCLASSIFIED	UL

Standard Form 298 (Rev. 2-89) (EG)
Prescribed by ANSI Std. 239.18
Designed using Perform Pro, WHS/DIOR, Oct 94

Final Technical Report

for AFOSR

Programmable Mesooptics with Resonant Near-Field Nonlinear Nanostructures

Sponsored by

Air Force Office of Scientific Research

Under Grant F-49620-98-1-0427

for Period 4/1/98 through 3/31/01

total: $390,000

Grantee

The Regents of the University of California, San Diego

University of California, San Diego

La Jolla, CA 92093

Principal Investigators: Y. Fainman
                                      (858) 534-8909

Program Manager: Dr. Gernot Pomrenke and Dr. Alan Craig

703-696-8426

2. Objectives/Statement of work

1. Develop modeling tools based on time-domain finite element/difference and rigorous coupled-wave analysis (RCWA) appropriate for periodic and non-periodic meso- and nano-scale structures.

2. Investigate the design, fabrication and characterization of meso-optic and resonant nanostructure devices that utilize Electro-optic (EO) and nonlinear (NL) composite artificial dielectrics.

3. Study near-field interactions between meso-scale devices in high-density applications as well as investigate their optical I/O to guided waves and to free space modes utilizing near-field phenomena.

3. Status of effort

1. We have developed finite difference analysis (FDA) for calculation of the electric field distributions created by nanostructured periodic and non-periodic electrodes. The calculated electric field distributions are used to acquire the refractive index modulation of EO devices. The results obtained with the FDA tool have been compared to those obtained from the finite element analysis (FEA) tool we developed previously, and found to be in good agreement.

2. For the studies of wave propagation through periodic meso-optic artificial .EO nanostructures, we have developed three-dimensional (3-D) RCWA that can model subwavelength surface relief periodic structures constructed of anisotropic materials. This newly developed tool has been integrated with the FEA and FDA calculations of refractive index non-homogeneity due to applied non-uniform DC electric fields or other nonlinear optical mechanisms for calculation of near- and far- field diffraction. We are in the process of evaluating the integrated modeling tools for different types of EO devices.

3. For the study of non-periodic meso-optic nanostructures, we have developed a time-domain-FDA (FD-TD) tool for calculating near-field optical wave propagation. The tool has been used to model the near-field diffraction of optical waves propagating through a single slit in a thick metallic sheet with dimensions comparable to the wavelength. Although the FD-TD modeling tool is based on an approximate solution that will, in theory, converge to the true solution when the grid spacing in the modeling domain is infinitely small, it is necessary to study the convergence criteria and the effect of imperfect absorbing boundary conditions. We have compared the FD-TD result to those calculated by a rigorous modeling tool: the Method of Moments (MoM).

4. To evaluate the applicability and accuracy of FD-TD for the modeling of periodic nanostructures, we initiated the investigation by comparing the results of FD-TD to those of RCWA. We are now in the process of identifying the best approach in FD-TD to treat the periodic boundary for normal incidence as well as conical incidence.

5. We have designed and fabricated a near-field artificial dielectric nanostructure constructed of an EO material substrate. The EO nanostructure acting as an EO modulator was patterned with subwavelength inter-digital electrodes on a bulk PLZT substrate using electron beam lithography. The structure was characterized with a He-Ne laser demonstrating EO modulation with only a zero diffraction order mode. We observed controllable phase changes in the incident laser beam due to the structure. An EO nanostructure made with embedded electrodes and EO materials with much lower

scattering loss (such as KTN) is under construction. We are also in the process of combining near-field artificial dielectric nanostructures with Fabry-Perot resonant structures such that we can construct a fast, low power and efficient EO modulator based on the near-field interaction in the device.

6. We have conducted a series of investigations on artificial nanostructured materials for optical nonlinearity enhancement in meso-optic systems. To study field concentration, accurate calculations of the fields inside the artificial resonant structures are necessary. We have developed an internal-field modeling tool by combining RCWA and our algorithm for efficient and accurate internal field representation. This tool has been used to design artificial nonlinear structures that simultaneously satisfy the phase matching condition and provide enhancement of the optical nonlinearity. Experimental characterizations of these structures are under preparation. To further enhance the optical nonlinearity of the designed artificial nonlinear structures, we employed ultrashort optical pulses as the light source, where the optical energy is confined in the time domain. We have extended the capabilities of RCWA to compute the internal and external fields of artificial dielectric structures with ultrashort pulse illumination, and apply them to investigate and design optical devices exhibiting transverse near-field localization. For comparison purposes, we have also used a direct time-domain modeling method (FD-TD) to model the artificial structures.

7. To fabricate devices more compatible with other devices in meso-optic systems in terms of materials and fabrication processes, we have studied different material compositions such as oxidized GaAs-AlAs (GaAs-AlO) nanostructures. We have fabricated GaAs-AlO and found an effective method to characterize the refractive index of oxidized AlAs. We investigate the optical properties of oxidized AlAs under different oxidation conditions. We have also explored the possibility of using the oxidation process to fabricate device structures that are difficult to fabricate with other processing techniques.

4. Accomplishments/New Findings

A. Modeling tool developments

The goal of this project is to conduct basic research towards the development of meso-optic diffractive optical elements (DOE) with programmability for application to optoelectronic and photonic systems. The first step toward understanding the near-field interactions inside EO and NL artificial nanostructured dielectrics and the near-field coupling between those structures in high-density applications is the development of modeling tools that can be used to accurately and efficiently model those near-field interactions. Accuracy and efficiency are the key elements in a successful modeling tool. The ability to model a structure of arbitrary geometry is also very important. Unfortunately, no single modeling tool can simultaneously achieve these three objectives. FD-TD is a potential modeling tool because of its flexibility and ability to model time-dependent optical phenomena. The accuracy of FD-TD for modeling non-periodic structures has been validated by many research groups, including ours. However, the accuracy of FD-TD for modeling periodic structures using only one cell and Floquet boundary conditions is still under investigation. The efficiency of FD-TD is another concern with limited computational resources. Other difficulties such as the accurate and efficient representation of dispersion in the modeling space and the random scattering from ferroelectric polycrystals might limit the use of FD-TD.

Our approach to develop viable modeling tools for meso-optic applications is developing, in parallel, tools based on RCWA suitable for modeling *periodic* structures and tools based on FD-TD suitable for modeling *non-periodic* structures. By comparing the results in those cases that can be solved by both tools as well as with the experimental results, we will be able to determine the criteria for choosing the most appropriate tool for a given structure.

(1) The modeling tools that we have developed for modeling *periodic* structure include:
  (i) Full 3-D far-field modeling for isotopic and anisotropic periodic artificial dielectrics based on RCWA.
  (ii) Effective and accurate near/internal field calculation by combining RCWA with our new internal field representation algorithm.
  (iii) The internal and external field calculation of artificial periodic dielectrics with ultrashort pulse illumination by extending the capabilities of RCWA.
  (iv) RCWA-FDA/FEA integrated modeling tool for EO periodic nanostructure modeling.

(2) The modeling tools that we have developed for modeling *non-periodic* structure include:
  (i) Rigorous modeling based on MoM.
  (ii) FD-TD.

Full 3-D far-field modeling

Full 3-D far-field modeling for isotopic periodic artificial dielectrics based on RCWA has been implemented and validated by comparison with experimental measurements (see figure 1). We have used the tool to design various artificial dielectrics with multi-functionality such as a form-birefringent computer-generated hologram (BCGH) and a nanostructured polarizing beam splitter (PBS). The new anisotropic version has been developed and compared to the analytical solution for non-grating cases and the experimental measurement of our BCGH and found to be in good agreement. The anisotropic version of RCWA has been used as the base to develop the RCWA-FDA/FEA integrated modeling tools for EO periodic nanostructures.

Integrated tool for EO periodic nanostructure modeling

The integrated tool performs the EO periodic nanostructure modeling in three steps. The first step is to use the FEA tool to calculate the static electric field distribution in the EO device structure where the nonhomogeneous electric fields as well as field localization are considered. In the second step, the non-uniform dielectric tensor resulting from the nonhomogeneous static electric field is calculated and averaged within each finite element cell. Because of the tensor property of the dielectric constant, the use of a vector field rigorous diffraction calculation is required. Finally the dielectric tensor is used as an input parameter for the anisotropic version of the full 3-D vector field RCWA calculation. With this three-step approach, we model the near-field interaction between the propagating optical wave and the nanostructured EO device. The results are compared to experimental measurements; this comparison is presented in the next subsection. The future direction of implementing a modeling tool for EO periodic nanostructure modeling is toward an all-in-one scheme where the static field modeling, the dielectric tensor calculation, and the 3-D full vector field modeling are done in one modeling method, such as time-domain FEA and FD-TD. The advantage of using one modeling method is to avoid the numerical error propagation from one method to another such that the accuracy and the efficiency of the modeling tool can be easily characterized. In order to implement the FD-TD for the EO periodic nanostructure modeling, we have developed FDA for calculation of the static electric field created by nanostructured periodic and non-periodic electrodes. The calculated electric field is used to acquire the dielectric tensor modulation of EO nanostructures. The result obtained by FDA tool has been compared to that obtained by finite element analysis (FEA) tool we developed previous and found to be in good agreement.

Efficient and accurate near/internal field calculation

We have conducted a series of investigations on artificial nanostructured materials for optical nonlinearity enhancement for use in meso-optic systems. To study field concentration, accurate calculation of the internal fields in the artificial resonant structures is necessary. We have developed an internal-field modeling tool by combining RCWA and our algorithm for efficient and accurate internal field representation. Our algorithm takes advantage of the internal symmetry of the grating in the longitudinal (z) direction—meaning that the eigenmodes of each layer will exist in pairs, with eigenvalues of opposite sign—and separate the eigenmodes according to the direction of stable propagation (i.e. the direction in which the real part of the complex phase argument decreases). The methodology we employ for the external solution also provides a relation between the mode pairs at each internal interface. Thus starting with the external field solution, we are able to solve for the modal amplitudes at each internal layer boundary. With the mode amplitude coefficients at each boundary known, we can compute the modal amplitudes at any arbitrary position in the grating by propagating each mode in the stable direction from the appropriate boundary:

$$A_i(\vec{r}_\perp, z, t) = \begin{cases} A_i(z_{n-1}) e^{\lambda_i(z - z_{n-1})} e^{-j(k_{i\perp} \cdot r_\perp - \omega t)} & \text{Re}(\lambda_i) < 0 \\ A_i(z_n) e^{\lambda_i(z - z_n)} e^{-j(k_{i\perp} \cdot r_\perp - \omega t)} & \text{Re}(\lambda_i) > 0 \end{cases} \qquad (1)$$

where $(\vec{r}_\perp, z, t)$ is the position of interest (in layer n), z_{n-1} and z_n are the locations of the layer boundaries ($z_{n-1} < z < z_n$), λ_i and $\vec{k}_{i\perp}$ are the longitudinal and transverse wavevectors of the ith mode in layer n, $A_i(\vec{r}_\perp, z, t)$ is the amplitude of the ith mode at the point of interest, and $A_i(z_{n-1})$ and $A_i(z_n)$ are the amplitudes of the ith mode at the respective boundaries. Thus, we are able to compute the field at any point in space inside the grating structure (see Fig. 1). The newly
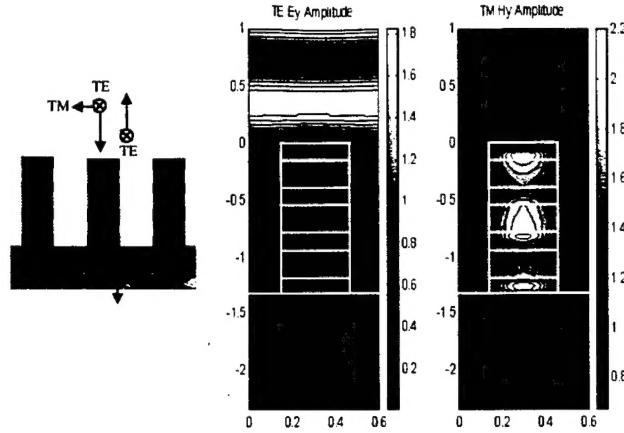
Figure 1. Near-/Internal field calculation of nanostructured PBS using RCWA based modeling tool.

developed internal-field modeling tool has been used to design artificial nonlinear structures that simultaneously satisfy the phase matching condition and provide enhancement of the optical nonlinearity.

Artificial periodic dielectrics modeling with ultrashort pulse illumination

We also developed a new method that extends the capability of RCWA to include ultrashort pulse illumination. To incorporate a Gaussian optical pulse, we represent the time-domain pulse as a finite superposition of plane waves with amplitudes satisfying:

$$F.T.\left\{ \bar{C}e^{-j(k_0 \cdot r - \omega_0 t)} \exp\left[-\frac{\left(t - \frac{\hat{k}_0 \cdot r}{v} - t_0 \right)^2}{2\tau^2} \right] \right\} = \bar{C}\sqrt{2\pi}\tau e^{-jk_0 r} \exp\left[-j(\omega - \omega_0)\left(\frac{\hat{k}_0 \cdot \bar{r}}{v} + t_0 \right) \right] \exp\left[-\frac{\tau^2(\omega - \omega_0)^2}{2} \right] \quad (2)$$

For each frequency, we solve for the grating interaction using RCWA, and then perform a coherent superposition of the fields of each frequency (from Eq. 1) at each point in space and time. With these improvements, the RCWA method becomes a powerful technique capable of computing the field at any time and at any point inside or outside the artificial dielectric, with monochromatic or ultrashort pulse illumination. Since we solve the diffraction problem for each frequency component separately, an arbitrary dispersion profile can be considered by simply modifying the dielectric constant of the grating structure for each frequency. The results are quite remarkable, and, for visualization, we can generate a movie of an optical pulse propagating within the artificial dielectric.

We use our previously studied near-field nanostructured PBS as an example for demonstrating the propagation of ultrashort optical pulses. Figure 2 shows three separate instances of a Gaussian ultrashort optical pulse (FWHM = 167 fs) propagating through the device. The polarizing beam splitter structure rests on a 100 µm thick substrate. The center wavelength of the pulse is at the design wavelength of the device (1.523 µm), and the peak of the incident pulse arrives at the input plane of the structure at t=0. In each figure, the pulse is incident from the bottom of the image, and each figure shows one period of an infinite periodic structure in the horizontal direction. As the depth of the beam splitter structure is much smaller than the spatial extent of the Gaussian pulse, Figures 2(a), (b), (e), and (f) are presented in wide views which show the overall pulse envelope as it propagates, while Figures 2(c) and (d) are close-up views which show the internal fields of the structure. Since the operating bandwidth of the device is much broader than the spectral bandwidth of the optical pulse, the performance of
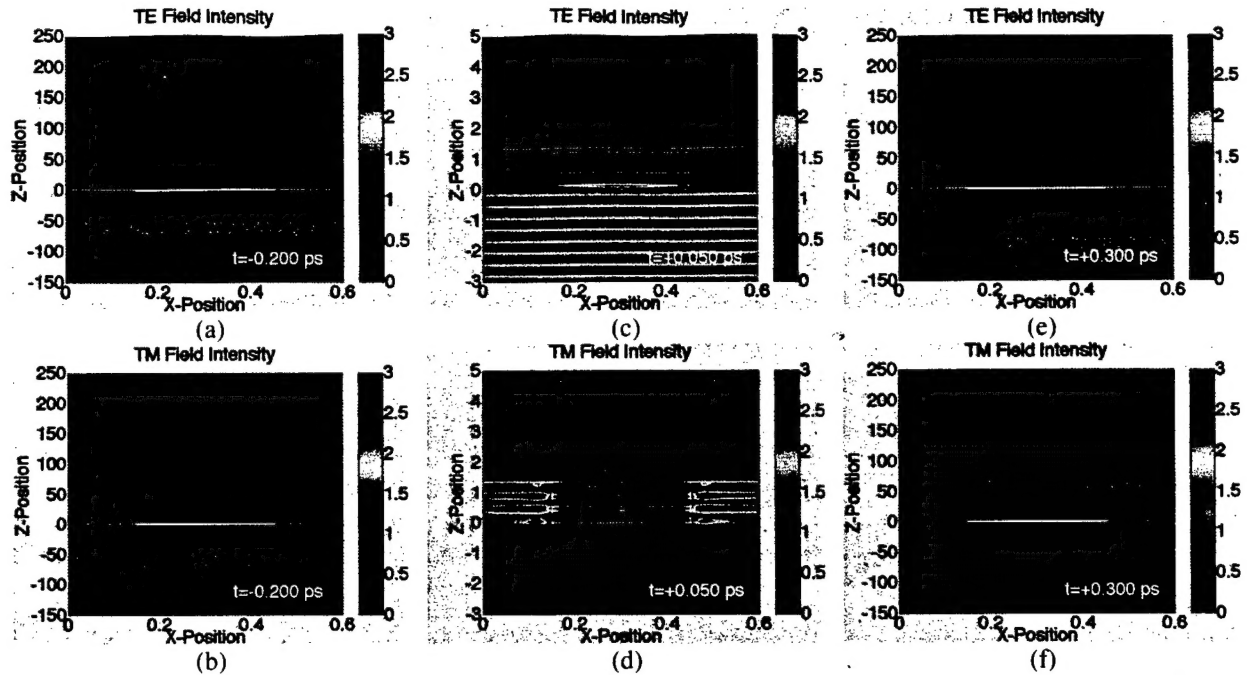
Fig. 2: Numerical modeling results of optical ultrashort pulses of TE (a, c, e) and TM (b, d, f) polarized beams incident onto a PBS nanostructure at (a, b) t=-0.2 ps, (c, d) t=0.05 ps, and (e, f) t=0.3 ps.

the device with the incident ultrashort pulse is essentially identical to the case of monochromatic illumination at the design wavelength: the TE polarization is fully reflected from the structure, while the TM polarization is fully transmitted into the substrate. Figures 2(a) and (b) show two pulses (TE and TM) before they enter the PBS. Figs. 2(c) and (d) show the two pulses propagating inside the PBS structure. For the TE polarization, since the wavelength is resonant with the structure, the pulse energy is unable to penetrate into the structure. The strong standing wave in front of the PBS is due to the interference between the reflected front portion of the pulse and the incident rear portion. For the TM polarization, the energy of the pulse is transmitted through the PBS structure. Inside the artificial dielectric structure, we see field concentration in the low index region. In the next section, we will discuss the application of this field concentration to enhance nonlinear optical effects in artificial dielectrics. Figures 2(e) and (f) show the two pulses propagating away from the PBS structure. It is clear that for the TE polarization, the pulse is totally reflected, and for the TM polarization, the pulse is fully transmitted. A QuickTime movie of the above results can be found on our website at http://uno.ucsd.edu/Research/Artificial/PBSPulse.shtml.

Non-periodic structure modeling: FD-TD vs. MoM

For the study of non-periodic meso-optic nanostructures, we have developed an FD-TD tool for calculating near-field optical wave propagation. Although the FD-TD modeling tool is based on approximate solutions of differential equations that will, in theory, converge to the true solutions when the grid spacing in the modeling domain is infinitely small, it is necessary to study the convergence criteria and the effect of non-perfect absorbing boundary conditions. The tool has been used to model Gaussian beams diffracted from a single-slit in a thick perfectly conducting screen. In our study, normally incident beams with Gaussian and constant profiles in space are used as light sources. The electric fields of the incident waves are polarized in the

direction parallel to the slit. The modeling space of the FDTD method can be divided into two parts: the workspace where the diffraction occurs and the absorbing boundary region where all the energy of the incident waves is absorbed. With the absorbing boundary region, E-M wave propagation in an infinite space can be simulated with the limited numerical space. The absorbing boundary condition in our model is the perfectly matched layer (PML). We have characterized the PML and find the optimal parameters for the lowest reflection coefficient. In our calculation, the near-field results of the continuous wave propagation in the frequency domain are extracted from the results of the pulse propagation in time domain via discrete Fourier transformation (DFT). The far-field diffraction pattern is then calculated by the near-to-far-field transformation. To study the accuracy of the FDTD method, we compare the FD-TD result to the results calculated by scalar theory (ST) and a rigorous theory (RT): MoM.

All the FDTD results shown above are using 20 layers in the PML where the difference between FD-TD and RT is about 1-2%. We find that sufficiently good results (difference between FD-TD and RT < 0.3%) can be obtained using only 5 layers in the PML when $L > \lambda$ and the slit is infinitely thin. With 40 layers, the difference between the results from FDTD and RT can be further reduced to 0.09% in the case shown in Fig. 4. The FDTD results using an incident beam with a Gaussian profile are always better than those of an incident beam with a constant spatial profile. This is due to the higher reflected energy from the PML for an incident beam with a constant profile. We can deduce from the results shown above that when the aperture of the slit
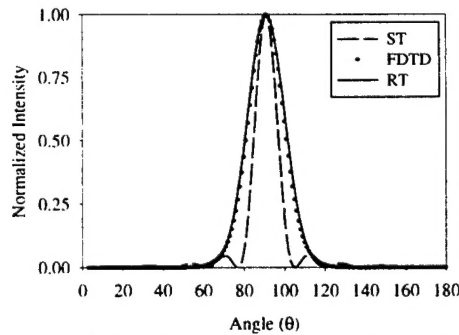

Figure 3 Far-field diffraction pattern of an incident beam with constant spatial profile through a finit-thickness slit in a perfect conductor (L=4.1λ)
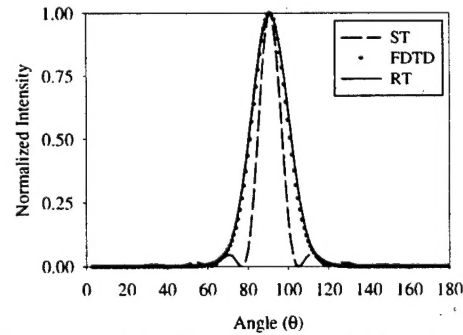

Figure 4 Far-field diffraction pattern of a Gaussian incident beam through a finite-thickness slit in a perfect conductor (L=4.1λ)
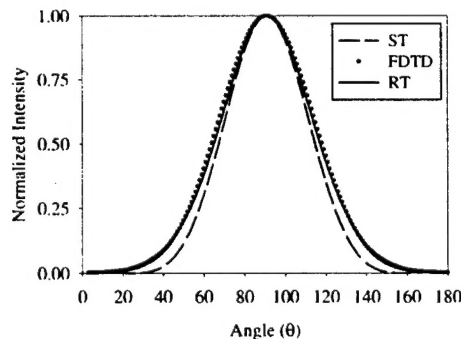

Figure 5 Far-field diffraction pattern of an incident beam with constant profile through a finite- thickness slit in a perfect conductor (L=1.1λ)

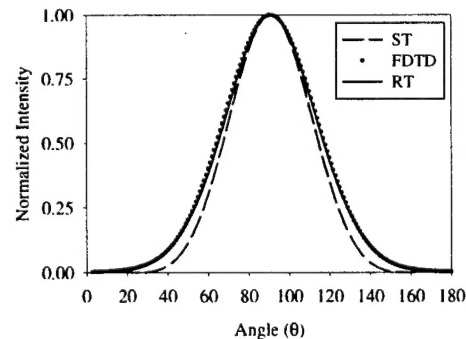Figure 6 Far-field diffraction pattern of a Gaussian incident beam through a finite-thickness slit in a perfect conductor (L=1.1λ)
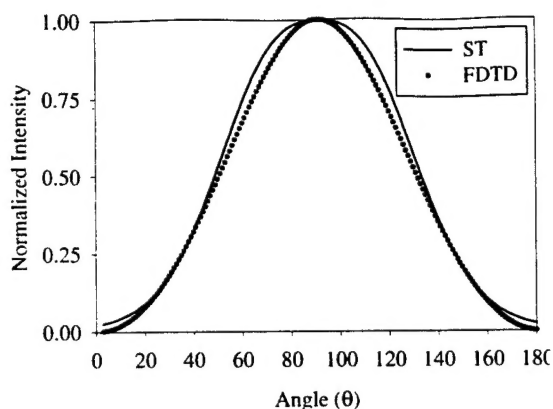
Figure 7 Far-field diffraction pattern of an incident beam with constant profile through a finite-thickness slit in a perfect conductor (L=0.4λ)
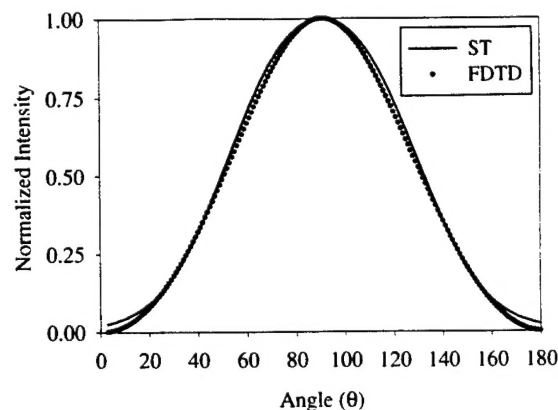
Figure 8 Far-field diffraction pattern of a Gaussian incident beam through a finite-thickness slit in a perfect conductor (L=0.4λ)

becomes smaller, the FDTD solution increases its sensitivity to the noise of the reflection in the PML. We obtain accurate results using the FDTD method in cases of apertures greater and smaller than the wavelength for incident beams with constant and Gaussian spatial profiles. Although the FDTD method is more computationally intensive, it has an advantage with respect to RT due to the simplicity of its formulation.

To evaluate the applicability and accuracy of FD-TD for the modeling of periodic nanostructures, we initiated the investigation by comparing the results of FD-TD to that of RCWA. We are now in the process of identifying the best approach in FD-TD to treat the periodic boundary for normal incidence as well as conical incidence.

Modeling of meso-scale devices in high-density applications: Parallel computing on Beowulf Class cluster parallel computer

Modeling meso-scale devices in high-density applications requires tremendous computing power (processor speed) and storage resources (memory and disk space), especially when subwavelength resolution is needed. In addition, the design optimization process relies on fast return time in the calculations. These requirements are difficult to fulfill with a single personal computer. Our study found that the modeling tools that we have developed are well suited to parallel computing. The eigenmode calculations in each thin layer in RCWA based modeling tools are completely independent. They can be executed on different processors (nodes) with non-shared memory and passing the result through fast Ethernet connection to the control unit for the final boundary condition matching processing. Because the memory needed for the eigenmode calculation is 16 times less than that needed for the boundary condition matching processing, each node requires much less memory than the control unit; therefore only one computer needs to have a high processing speed and a large amount of memory. These types of calculations present lowly parallel processing and can be easily implemented on loosely coupled multiple-instruction multiple-data (MIMD) computers such as Beowulf Class cluster parallel computers. When calculating short pulse illumination using RCWA based modeling tools, each frequency component can also be calculated individually. For our FD-TD modeling tools, the parallelism can be higher and memory can be used more efficiently.

We have tested and successfully linked three nodes (three 6th-generation x86 processors) in our parallel system using a small numerical test program and an evaluation version of a commercially available message passing interface software from MPI software Technology under Windows NT environment. Our goal is to include 12 nodes and one control unit connected through a 100Mb/s LAN for intensive modeling. We are now in the process of transferring our exiting computer code of the modeling tools to parallel code that is suitable for the newly established cluster parallel computer. Working codes in parallel format will be ready for testing shortly. After the implementation, our design and modeling ability will be significantly increased.

B. EO and NL composite near-field artificial dielectrics in meso-optical systems: design, fabrication, and characterization

(1) EO near-field artificial dielectrics

We have designed, fabricated, and characterized a near-field artificial dielectric nanostructure constructed on an EO material substrate. The nanoscale inter-digital electrodes are fabricated using electron beam lithography. A 100 nm thick high molecular weight (950K) PMMA (MicroChem Corp., MA) was spin-coated on a PLZT (8.8/35/65) substrate. A Cambridge S360 scanning electron microscope controlled by NPGS system (JC Nabity Lithography Systems, MT) was used as the pattern definition tool. The area of the pattern is 90 µm x 90 µm. The electrodes have a 600nm period with linewidth of about 100nm. After the pattern was developed, a 5nm thick Cr layer plus a 15 nm thick Au layer were thermally deposited on the patterned surface. Figure 9 shows the SEM micrograph of the edge of the grating/electrode pattern after the metal layer was deposited. The electrode patterns were obtained by lifting off the resist in acetone with the assistance of ultrasonic waves. Figure 10 is a schematic diagram of PLZT crystallites. The grain size of the PLZT is about 10 µm. Most of our electrodes are located on a single grain PLZT crystallite.

This modulator was designed to have only two opposing input voltages. The two 150µm x 50 µm input pads were defined together with the electrodes. These input pads were wire-bonded to a chip carrier. The device was tested with a He-Ne laser. Due to the subwavelength periodicity, only the zero diffraction order should exist as a propagating mode. As expected, we only observe one diffraction order in the far field.
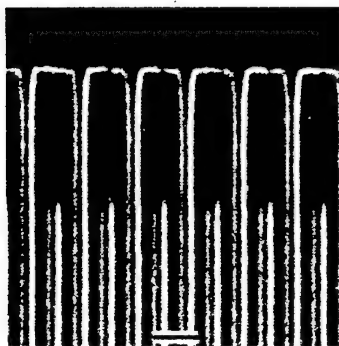

Figure 9. SEM micrograph of the fabricated inter-digital electrodes pattern. The scale bar in the photograph is 1 µm.
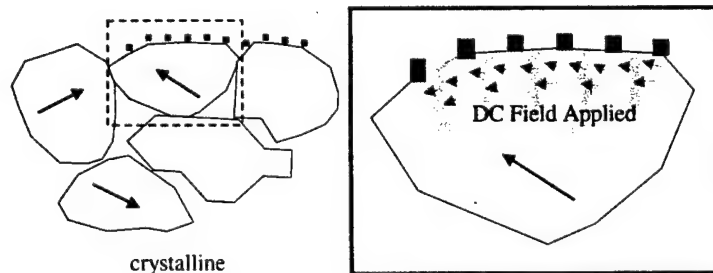
Figure 10. Schematic diagram of PLZT crystallites with surface electrodes. The insert shows one grain of the crystalline. The electric field can only penetrate less than one grain deep.

We use a Jones matrix to characterize the modulator as $J_M = \begin{bmatrix} a & 0 \\ 0 & be^{j\phi} \end{bmatrix}$, where a and b are the amplitude transmittance for the two orthogonal linear polarizations, and ϕ is the phase delay between the two polarizations when light propagates through the device. PLZT has a polycrystalline structure and ϕ is zero without an externally applied electric field. The modulator is introduced into the characterization setup such that the electrodes lie in the horizontal direction. The transmittance (including reflections from the PLZT surfaces) for the two orthogonal linear polarizations (horizontal and vertical), a and b, were measured to be 0.530 and 0.432, respectively. The refractive index of the PLZT substrate is 2.5. Taking into account the reflection from the two PLZT surfaces which is 33.4% total, one can measure and determine that the absorption loss caused by the metal electrodes are about 20% and 35% for the horizontal and vertical polarizations, respectively. With a simple polarimetry setup as shown in Fig 11, we study the phase retardation introduced by the modulator with applied external fields. Because of the different transmission coefficients for horizontal and vertical polarizations, the analyzer before the photodetector has to be rotated by a couple of degrees to get the minimum total transmittance. Figure 12 illustrates the transmitted intensity variation as a function of applied voltage. From the measurements, we calculated the maximum phase delay ϕ introduced by the structure at 25 V driving voltage to be 5.5 degrees. The refractive index change is then calculated to be 0.015 based on the assumption that the penetration depth is the same as the grating period (see Fig. 13). It is known that PLZT introduces scattering
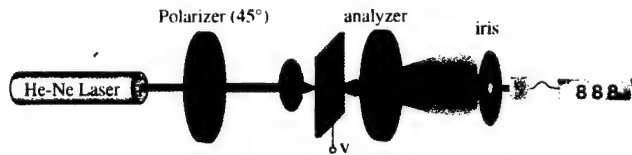

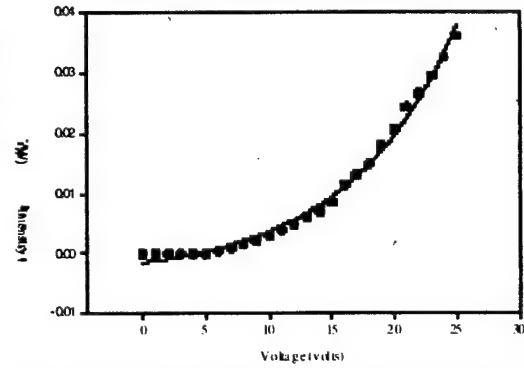Figure 11. Experimental setup for characterizing the modulator.

Figure 12. Light intensity through a pair of cross polarizers as a function of driving voltage on the modulator.
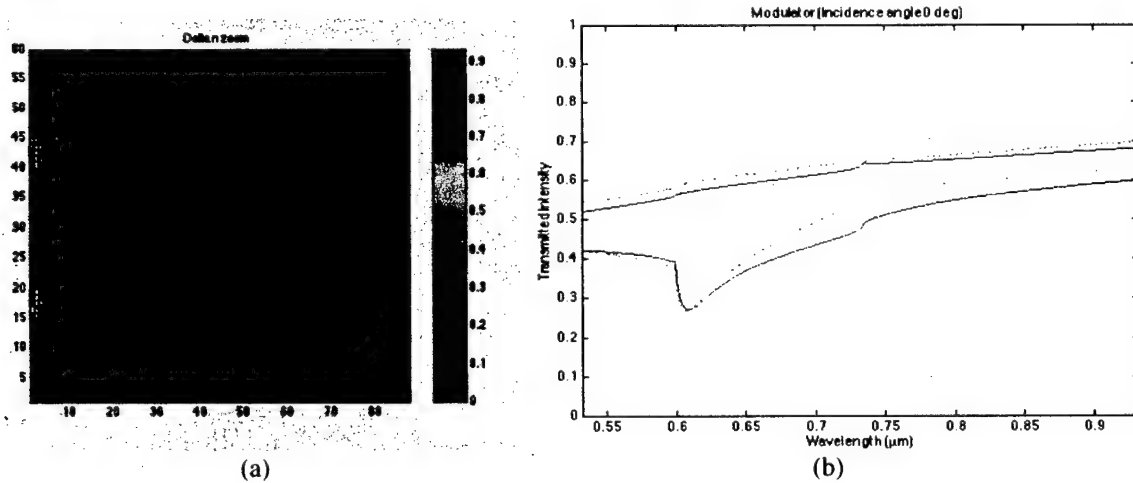

(a)

(b)

Figure 13. Modeling of the modulator. (a) FDA calculation of index modulation, (b) RCWA transmission calculation. Dashed line: no electric field applied; Solid line: with electric field; Red: TM polarization; Blue: TE polarization.

and depolarization under strong electric field. However, no visible scattering was observed with this applied voltage. In addition, the iris in front of the detector in our setup eliminates the scattering, if there is any, and proves the effect being polarization rotation.

The currently achieved phase change is not sufficient for making any useful device. We are preparing samples using EO crystals. The metal surface electrodes will be replaced by transparent embedded ITO electrodes, which will increase the phase change noticeably. By creating a resonant structure such as a Fabry-Perot electrooptic modulator, we can construct a fast, low power and efficient EO modulator based on the demonstrated EO modulation.

(2) Nonlinear composite near-field artificial dielectrics

Nonlinearity Enhancement in composite near-field artificial dielectrics

We have studied nonlinearity enhancement in composite near-field artificial dielectrics. Nonlinearity enhancement using optical nonlinear nanostructured artificial dielectrics can be achieved simultaneously employing two different enhancement mechanisms: high field concentration provided by the polarizability of the engineered nanostructure, and high peak power provided by ultrashort optical pulses. Optical nonlinearities are significantly enhanced by the high peak powers achieved through time localization using ultrashort pulse laser sources. We found that an additional enhancement of optical nonlinearities can be achieved by engineering nanostructured artificial dielectrics that will provide spatial field localization in addition to temporal localization. Figure 14 shows modeling results illustrating an important near-field phenomenon: localization of the field in the transverse direction in an artificial dielectric structure. The nanostructured artificial dielectric is a square grating with a period of 0.69 λ and duty ratio of 10%. The refractive indices of the material and air are assumed to be 3.0 and 1.0, respectively, and the depth of the structure is 100 λ. The incident pulse is incident from below in each frame (the pulse peak arrives at the incident face of the structure at t=0), and is polarized in the TE orientation. Each frame shows one period of an infinite periodic structure, with the high index region at the center of the figure. Figure 14a shows the incident pulse approaching the structure. Figure 14b shows the pulse propagating inside the artificial dielectrics. Note that although the incident pulse has a uniform transverse profile. inside the structure the field is localized in the high index material. The peak field intensity inside the artificial dielectric is approximately 10 times that of a pulse propagating through a bulk material of the same index. This field concentration is due to the near-field effects in the artificial dielectric, and exists only inside the structure—the transmitted and reflected fields will have uniform transverse profiles (see Fig 14c).
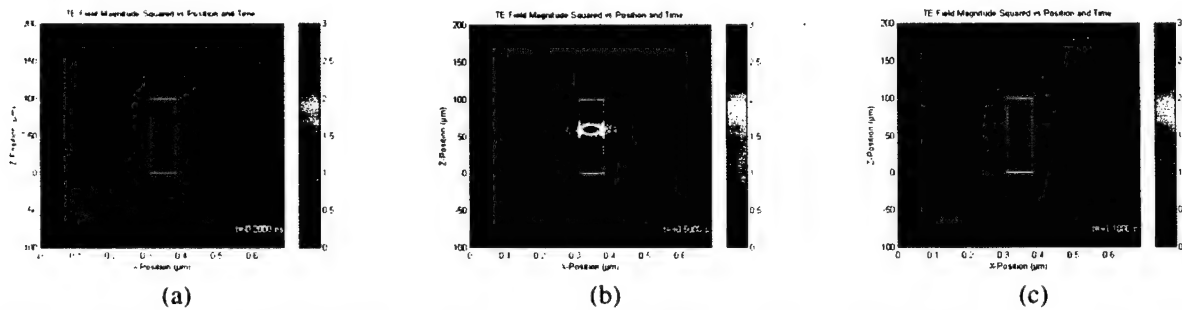

(a) (b) (c)

Figure. 14. Numerical modeling results showing a TE polarized ultrashort pulse propagating through a subwavelength grating: (a) t=-0.20 ps; (b) t=+0.50 ps, note inside the grating the field exhibits transverse localization in the high index region; (c) t=+1.10 ps.

Disregarding the detailed mathematical description of the nonlinear properties of artificial nanostructures, the stronger effective nonlinear susceptibilities can be intuitively explained as the result of the stronger average macroscopic nonlinear polarization, which is simply a volume average of the mesoscopic (compared to the atomic scale) nonlinear polarization in each constituent material. Because the mesoscopic nonlinear polarization is proportional to the square of the mesoscopic E-field for the $\chi^{(2)}$ term, the mesoscopic nonlinear polarization can be strongly intensified with high field concentration. Therefore, the volume average of the mesoscopic nonlinear polarization (i.e. the macroscopic nonlinear polarization) and the effective susceptibilities in artificial nanostructures can exceed those in the constituent bulk materials.

Phase Matching with Nonlinear composite near-field artificial dielectrics

We have investigated two phase matching approaches based on the unique properties of artificial dielectrics: form birefringence and dispersion manipulation (photonic crystals), which will be used to increase the efficiency of nonlinear frequency conversion and eliminate the walk-off of the conventional phase matching method. The first approach utilizes the form-birefringence property of artificial dielectrics. According to second-order effective medium theory, the effective indices depend on the period and the fill factor of the artificial dielectrics:

$$n_{TE}^{(2)} = \left\{ n_{TE}^{(0)2} + \frac{1}{3}\left(\frac{\Lambda}{\lambda}\right)^2 \pi^2 F^2 (1-F)^2 \left(n_3^2 - n_1^2\right)^2 \right\}^{1/2}$$

$$n_{TM}^{(2)} = \left\{ n_{TM}^{(0)2} + \frac{1}{3}\left(\frac{\Lambda}{\lambda}\right)^2 \pi^2 F^2 (1-F)^2 \left(\frac{1}{n_3^2} - \frac{1}{n_1^2}\right)^2 n_{TM}^{(0)6} n_{TE}^{(0)2} \right\}^{1/2}$$

(3)

With effective indices caused by the artificial dielectrics, anisotropic crystals (in this case, LiNbO₃), that were phase matched using a conventional method at a particular direction of propagation where the nonlinearity is low, can be phase matched in the direction of higher nonlinearity of the crystal (e.g. materials with large d_{13}) (see Fig. 15). The subwavelength artificial dielectric in a LiNbO₃ crystal creates equal effective indices for second harmonic TE wave and fundamental TM wave when the fill factor is close to 95%. In addition, since the propagation direction is tuned to be perpendicular to the optic axis of the bulk crystal, the walk-off between the energy front and wave phase front is eliminated. Due to the large artificial birefringence achievable with artificial dielectrics, this approach can also be used to achieve phase matching in low birefringence crystals where the phase matching condition cannot be fulfilled with conventional phase matching methods. The second-order effective medium theory (see Eq. 3) also shows us that when the grating period is comparable to but smaller than the wavelength, we can change the fill factor by adjust the grating period to achieve the same
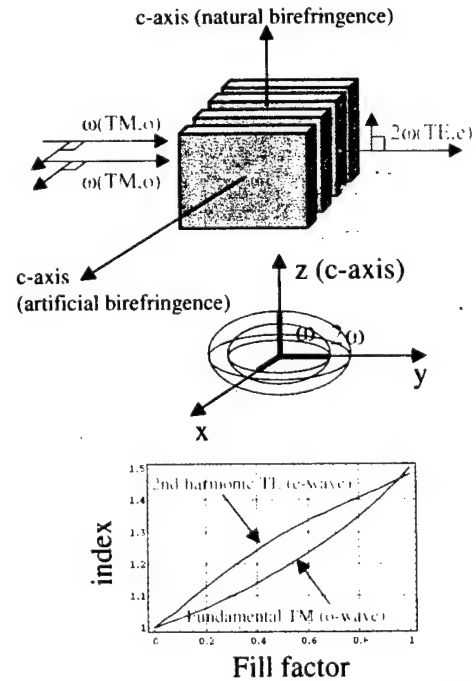

Figure 15. Nonlinear phase matching based on the form-birefringence effect of artificial dielectric. The simulation shows that the phase-matching can be achieved through controlling the grating fill factors.

phase matching. With this design flexibility combined with the field concentration property of artificial dielectrics, we can achieve phase matching and nonlinear enhancement simultaneously. The design of this structure is under investigation.

The second approach utilizes the photonic crystal property of artificial dielectrics, where the dispersion relation can be manipulated by changing the geometric structure of the artificial dielectric. Collinear phase matching can be achieved for wave frequencies near the photonic bandgap where large artificial dispersion (either negative or positive depending on which side of the bandgap) appears, if the material dispersion is compensated by the artificial dispersion. By adjusting the period and shape of the photonic crystal, this condition can be fulfilled. Non-collinear phase matching can also be achieved if the following conditions are satisfied:

$$\omega_{2nd} = \omega_{fundamental} + \omega_{fundamental}$$
$$k_{2nd} = k_{fundamental} + k_{fundamental} \pm nK$$

(4)

ω is the frequency, k is the wave vector of the optical wave, n is an integer, and K is the grating vector defined as $2\pi/\Lambda$. The phase matching direction mainly depends on the orientation of the photonic crystal, which can be tuned to coincide with the direction of the highest nonlinearity of the bulk crystal. The flexibility and low-loss properties of this approach to achieving phase matching are very useful for high efficiency nonlinear processing. The subwavelength scale of the artificial dielectric structure can further increase nonlinear effects due to strong field concentration inside the structure.

To construct a photonic crystal for the study of nonlinear phase matching, we have investigated different structures and considered their ease of fabrication. We found that multilayer periodic nanostructures (e.g., see Fig. 16a) possess a broad reflectance band for TE polarized waves over a wide angular range. This property and the device geometry are analogous to 2-D photonic crystals (see Fig. 16b). In contrast to conventional 2-D photonic crystals constructed of two materials, our MPN-based 2-D photonic crystal is constructed of three materials (i.e., air, high index and low index dielectrics). The three-material design has an advantage in terms of ease of microfabrication of large aperture devices necessary for long interaction length devices and/or free space optics applications. A 3-D cubic structure can be built by etching a 2-D binary grating into a multilayer mirror.

To design a photonic crystal with three materials, we use EMT as a design tool similar to the method that was used in [19]. Later, we use RCWA to validate the EMT design. The RCWA modeling result of Fig. 17 shows the clear existence of a high reflection band falling between 1.4

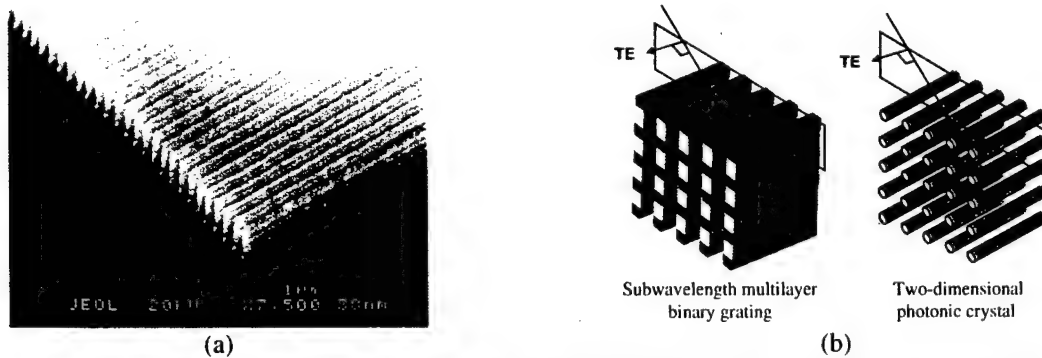Subwavelength multilayer binary grating   Two-dimensional photonic crystal

(a)   (b)

Figure 16. (a) SEM micrograph of a multilayer artificial dielectric nanostructure, and (b), subwavelength multilayer binary grating and two dimensional photonic crystal analogy.
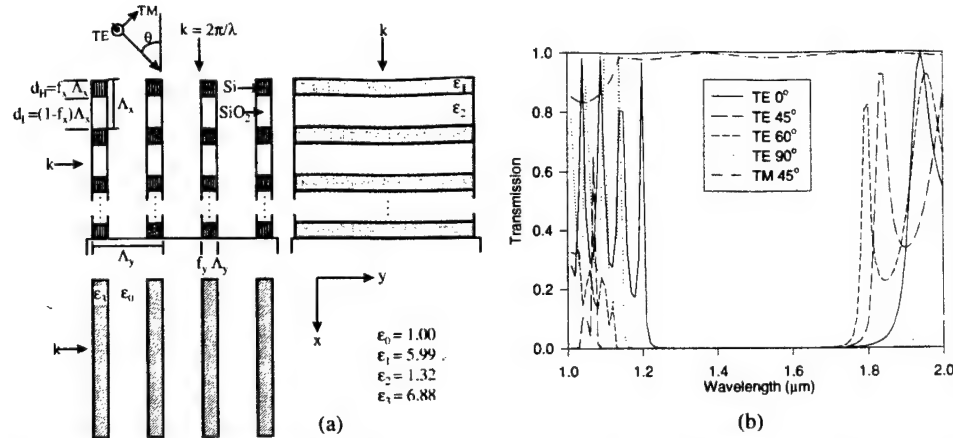
Figure 17. (a) Schematic diagram of a 2-D 13-layer three-material photonic crystal and its effective multilayer thin film stacks in vertical and horizontal directions. (b) RCWA results of transmission vs. wavelength for different incident angles. TE 90° represents the results for incidence from the y direction.

μm and 1.6 μm. It also shows that, at a 45° angle of incidence, the structure is transparent for TM and reflecting for the TE polarized light, demonstrating the use of this type of design for PBS application.

We also calculate the band structure of the crystal and find a full forbidden band for the TE polarized waves (see Fig. 18). No full forbidden band for TM polarized waves overlaps with that of the TE polarized waves; therefore, this crystal does not have a complete band gap. This is a common property of 2-D photonic crystals with a rod as the base element. One interesting feature of this crystal is that from the point x to s in the Brillouin zone (corresponding to 0° to 47° to the surface normal) the forbidden bands for TE and TM are completely separated. This means that in the frequency range from 0.25 to 0.4, and the incidence angle range from –47° to 47°, the TE field will be reflected and TM field will be transmitted. The feature of broad spectral and angular bandwidths makes the three-material photonic crystal suitable for multispectral polarization optics imaging applications.
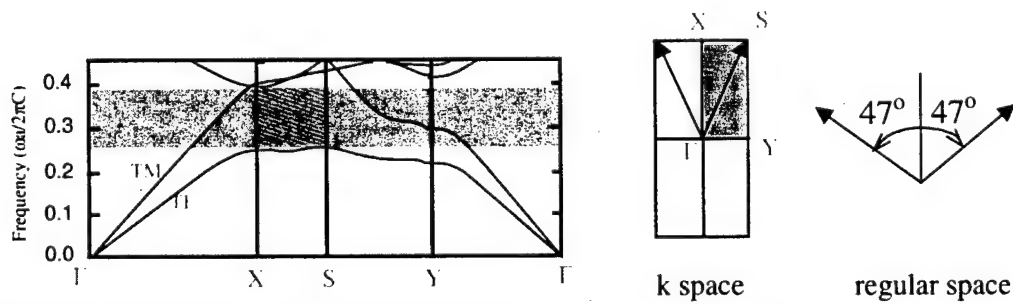

Figure 18 Photonic band structure of a 2-D 13-layer three-material photonic crystal

Characterization of Oxidized GaAs-AlAs nanostructure

We have studied an alternative material composition that is more compatible with other EO devices in meso-optics systems in terms of materials and fabrication processes. We are particularly interested in the optical properties of oxidized GaAs-AlAs multilayer structures. Through the oxidization, the refractive index of AlAs is decreased considerably where the

refractive of GaAs remains intact; therefore the index ratio of GaAs-AlAs pairs is largely increased. This type of material composition is especially suitable for constructing three-material photonic crystals, because the surface relief grating can be fabricated before the oxidation of AlAs. Although the wet oxidization process of AlAs is fairly standard, the refractive index of the generated Al_xO_y that was measured by different groups is inconsistent. The reported refractive index of oxidized AlAs ranges from 1.55 to 1.75. There are several possible reasons for the differing results. First, full oxidation of AlAs is difficult to achieve. Typically, partially oxidized AlAs has a higher refractive index than fully oxidized AlAs. Second, depending on the geometry of the AlAs structure (size and thickness), the full-oxidation condition may be different. To ensure full-oxidation, the size of our GaAs-AlAs multilayer structure is limited to less than 100 × 100 μm. With such a small size, conventional methods such as ellipsometry cannot be used to characterize the refractive index of AlO because of the alignment problem. The absolute reflectance measurement method is also very difficult to perform because the method requires plane wave incidence and significant noise will be generated due to scattering from the edges of the structure. The third reason is that during the oxidation process not only does the refractive index of AlO change, but the thickness of the AlO layers also decreases, adding error to the refractive index characterization process.

We have fabricated GaAs-AlO multilayer structures and found an effective method to characterize the refractive index of oxidized AlAs. Our approach to overcome the scattering noise from the edges is to measure the relative reflectance from a VCSEL-like cavity. If the test subject is a multilayer mirror, it will be very difficult to fully characterize the refractive index and thickness with the this kind of relative reflectance measurement since the reflectance band is generally very broad and not well-defined. However, for a structure similar to a VCSEL cavity, a dip will appear on the reflectance spectral band. The position of the dip is determined by the refractive index and the thickness of the layers. Since the shape of the dip is usually very sharp when the multilayer structure has high reflectivity, the dip is resolvable in the relative reflectance measurement and its position is easy to locate even though the scattering noise appears. It is fairly easy to match the position of the dip in the simulated result with estimated index and thickness values, to the measured result. For example, we have characterized a sample of the cavity depicted in Fig. 19(a) by using a tunable Argon-pumped Ti:Saphire laser. The measured results are plotted in Fig. 19(b). We can clearly see the sharp dip on the reflectance band. We chose refractive index of 1.63 at the wavelength of 845nm and thickness reduction of 12%
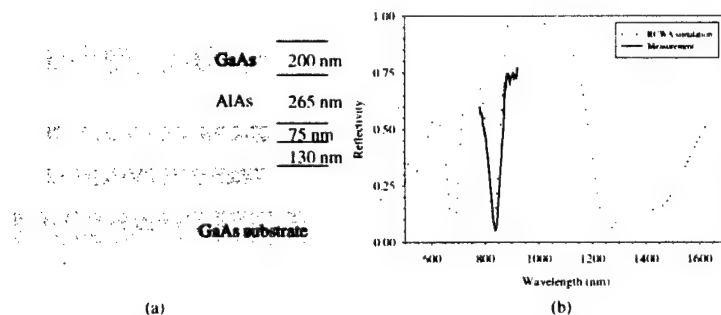

Figure 19. (a) Schematic diagram of GaAs-AlAs cavity used for AlO refractive index characterization. The design parameters are indicated in the figure. (b) The measured and the calculated reflectivity vs. wavelength. The refractive index of 1.63 at the wavelength of 845nm and thickness reduction of 12% are used for calculation
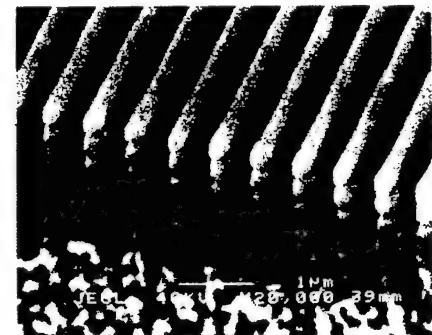
Figure 20. SEM photograph of the fabricated multilayer binary grating. The grating is fabricated on a GaAs substrate consisting of multilayer structure of GaAs and AlO.

estimated from SEM photograph as the parameters for our simulation. We found the dip in the simulated result (see Fig. 19b) matched the one in the measurement quite well. Although the method will not provide deterministic results on the index and the thickness, it narrows down the range of possible values for the index and thickness. More research on accurate thickness measurement approaches is needed to determine the true refractive index of AlO. In addition to the advantage of reducing the measurement error caused by the diffraction noise, our approach for the refractive index characterization possesses another important advantage. We can determine the refractive index for a specific operating wavelength where the dip centers simply by matching the sharp dip on the reflectance band instead of matching the whole flat reflectance band. The dip's location is very sensitive to any small change in the refractive index because it results from a resonance with very high Q-factor.

In addition to the cavity structure, we also fabricated another sample (see Fig. 20) to explore the possibility of using GaAs-AlO for constructing multilayer periodic nanostructures. The thickness of each layer is chosen to satisfy resonance in the near IR spectral range and the grating period is 0.6μm. We can clearly see the shrinkage of the oxidized AlAs. The sample was fabricated by first depositing a GaAs-AlAs multilayer structure and then etching a binary subwavelength grating into the multilayer structure. Finally the AlAs was wet oxidized. Compared to the original Si-SiO$_2$ multilayer grating, this new structure is much easier to fabricate. We conclude that the oxidized GaAs-AlAs multilayer structure is a good candidate for constructing a three-material photonic crystal. In addition, we have studied the refractive index profile of the oxidized AlAs to investigate the possibility of using oxidized GaAs-AlAs in a waveguide structure or other devices in meso-optics applications. We found that the oxidation process leaves a fairly sharp index change between oxidized and non-oxidized AlAs. No large area index gradient is observed. A nonlinear composite artificial dielectric waveguide structure based on GaAs-AlAs material composition is under preparation for characterization of the field concentration, nonlinear enhancement, and phase matching properties of artificial dielectrics.

C. Near field interactions between the meso-scale devices in high-density applications

We have studied two cases: (i) near-field interaction between periodic meso-scale devices in the wave propagation direction, (ii) near-field interaction between periodic meso-scale devices in the transverse direction. The first case is a design for an integrated device, which is a color selective (< ~50 nm), broad angular bandwidth (~ ±45°) filter and also exhibits field concentration for improved detection efficiency. The filter is constructed by integrating a 1-D multilayer structure with an artificial dielectric nanostructure (period 0.45 λ, duty 10%). Fig. 21 shows the internal and near fields of the device for the case of monochromatic illumination at the resonant wavelength and normal incidence. The mode structure of the photonic crystal is altered by the adjacent 1-D multilayer structure. The electric field has been localized in the last layer of the artificial nanostructure, resulting in a near field amplitude that is much greater than that of the transmitted field.
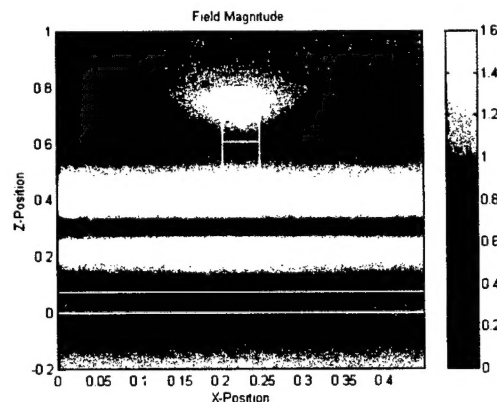

Figure 21. Field localization in the last layer of a multifunctional artificial dielectric device. The device is periodic in x; only one period is shown.

The second case is a 2-D photonic crystal structure with periodic defects (see Fig. 22). Such a structure exhibits very strong field concentration at the location of the defect for a very narrow range of frequencies over a large angular bandwidth. We observed strong near-field interaction between adjacent defects that modifies the electric field in the transverse direction. This structure can be used as a receiver structure exhibiting narrow frequency selectivity, broad angular sensitivity, and enhanced detection efficiency. A transmitivity of the structure is shown in Fig. 23. The periodic defects introduce a narrow transmission band into the broad reflectance band of the original photonic crystal.
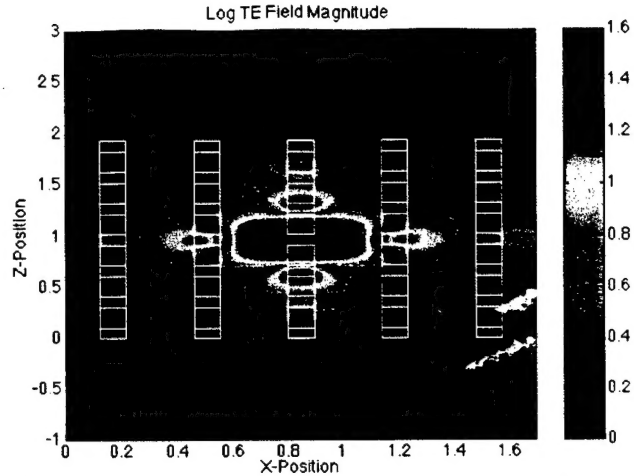

Figure 22. Field Magnitude (log scale) inside and near one period of a three material 2-D photonic crystal structure with a defect every fifth lattice period. Note the strong field concentration inside the structure at the location of the defect.
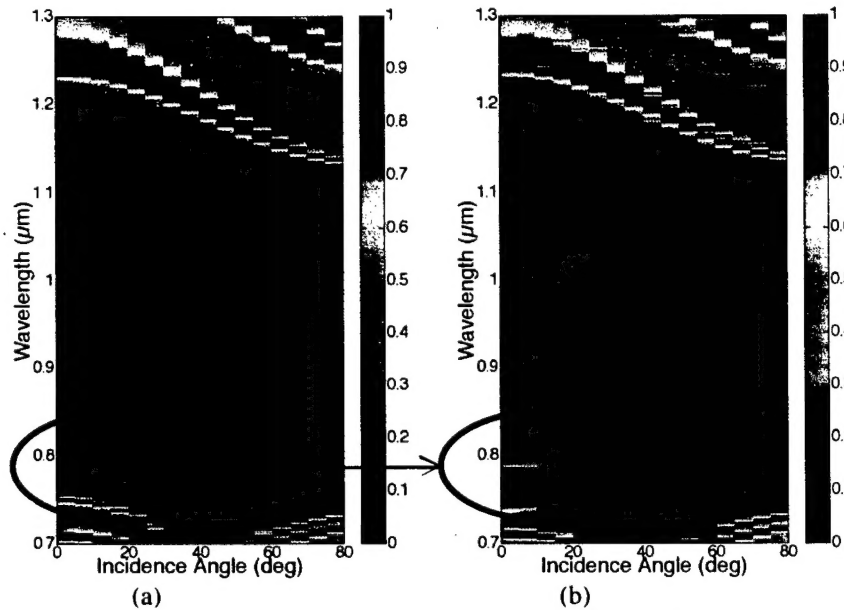

Fig. 23. Transmittivity as a function of incidence angle and wavelength of (a) a 2-D photonic crystal without defects and (b) the filter structure shown in Fig. 2. The introduction of the periodic defect permits transmission of a narrow range of wavelengths for a wide range of incidence angles.

For characterization of the near field interactions between non-periodic meso-scale devices and optical I/O to guided waves and to the free space modes utilizing near-field phenomena, we use tools based on FD-TD. Its performance has been compared with the RCWA using same structure. The modeling results using both methods have been compared and found in good agreement.

D. Rigorous Enhancement of Nonlinear Optical Phenomena: Second Harmonic Generation

To develop a tool capable of modeling nonlinear effects in nanostructures, we modify our modeling approach to incorporate the nonlinear polarization. As a first step in reaching this goal, we have extended our RCWA-based modeling tools to investigate SHG in the undepleted pump approximation. Using the undepleted pump approximation, we first assume that the nonlinear polarization includes only the SHG term:

$$\bar{P}_{NL}(\bar{r},t) = \frac{\chi^{(2)}}{2} \bar{E}_\omega \bar{E}_\omega. \tag{5}$$

Consequently, we are able to effectively decouple the fields at the fundamental and harmonic frequencies. We first determine the fields at the fundamental frequency using the standard RCWA technique, and then use these results to obtain the nonlinear polarization for the fields at the second-harmonic frequency. The equations describing the fields at the second-harmonic frequency are given by:

$$\nabla \times \bar{E}_{2\omega} = -\mu \frac{\partial \bar{H}_{2\omega}}{\partial t} \tag{6a}$$

$$\nabla \times \bar{H}_{2\omega} = \varepsilon_{2\omega} \frac{\partial \bar{E}_{2\omega}}{\partial t} + \frac{\partial}{\partial t} \bar{P}_{NL}(\bar{r},t). \tag{6b}$$

Using a modified form of the RCWA technique, Eqs. 6a and 6b can be reduced to a system of coupled first-order inhomogeneous differential equations. The resulting governing equation is:

$$\frac{\partial}{\partial z} \begin{vmatrix} \bar{S}_x^{(2\omega)}(z) \\ \bar{S}_{yx}^{(2\omega)}(z) \\ \bar{U}_x^{(2\omega)}(z) \\ \bar{U}_y^{(2\omega)}(z) \end{vmatrix} = [A_{2\omega}] \begin{vmatrix} \bar{S}_x^{(2\omega)}(z) \\ \bar{S}_{yx}^{(2\omega)}(z) \\ \bar{U}_x^{(2\omega)}(z) \\ \bar{U}_y^{(2\omega)}(z) \end{vmatrix} + \begin{vmatrix} \bar{Y}_{Sx}^{(2\omega)}(z) \\ \bar{Y}_{Sy}^{(2\omega)}(z) \\ \bar{Y}_{Ux}^{(2\omega)}(z) \\ \bar{Y}_{Uy}^{(2\omega)}(z) \end{vmatrix} \tag{7}$$

where $\bar{S}_x^{(2\omega)}(z)$, $\bar{S}_{yx}^{(2\omega)}(z)$, $\bar{U}_x^{(2\omega)}(z)$, and $\bar{U}_y^{(2\omega)}(z)$ are vectors containing the transverse spatial Fourier expansion coefficients of $E_{x\,2\omega}$, $E_{y\,2\omega}$, $H_{x\,2\omega}$, and $H_{y\,2\omega}$, respectively; the matrix $[A_{2\omega}]$ represents Maxwell's equations and the material and geometric properties of the nanostructure; and $\bar{Y}^{(2\omega)}(z)$ is the inhomogeneous term corresponding to the nonlinear polarization. We solve Eq. 7 using standard techniques and apply the appropriate boundary conditions to obtain the transmitted and reflected field mode amplitudes at the second-harmonic frequency.

For simplicity, we first analyze SHG enhancement in a thin nanostructure with a monochromatic incident field. Fig. 24 shows a thin structure with a depth $d = 0.29\lambda$ such that the effects of material dispersion will be minimal. The field magnitude squared ($|E|^2$) for a normally incident monochromatic wave at the fundamental frequency propagating inside the structure is shown in Fig. 25. Strong field localization in the high refractive index material is observed inside the nanostructure. The amplitude of the incident wave is selected to ensure that the amplitude of the second-harmonic wave does not exceed approximately 1% of the incident field, satisfying the undepleted-pump approximation. Using the modified RCWA approach which includes the undepleted-pump SHG nonlinear polarization, we model the output of the SHG process and compute an enhancement factor by normalizing the nanostructure SHG transmitted intensity output to that of the bulk material case (F=1.00). In contrast to approximate methods, our technique takes into account longitudinal effects in the nanostructure, and yields an enhancement factor of approximately 2.17 for the structure shown in Fig. 2. Thus, due to near-field localization in the nanostructure, the SHG output of the nanostructure is greater than that of

a bulk material of the same thickness. In the future, we will extend the nonlinear RCWA tools to include the time-domain Fourier decomposition and field superposition technique described above, in order to analyze SHG in nanostructures for incident ultrashort optical pulses.
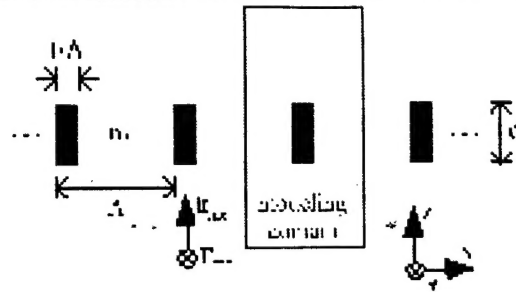

Fig. 24. Schematic diagram of the 1-D periodic SHG enhancement structure ($\Lambda = 0.65\lambda$, F=0.09, $d = 0.29\lambda$, $n_1 = 3.5$, and $n_2 = 1.0$). The incident illumination is a normally-incident monochromatic plane wave with wavelength λ.
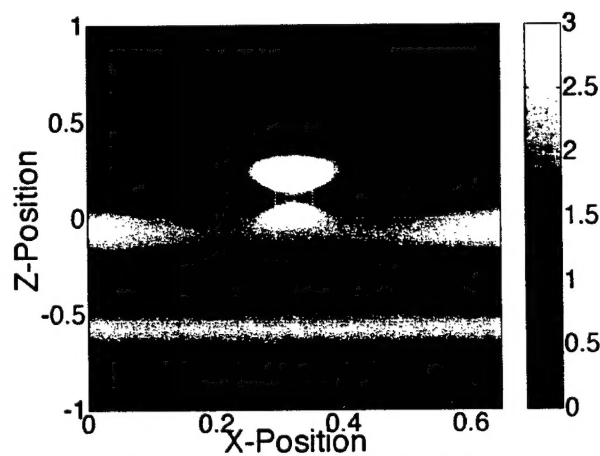

Fig. 25. Field magnitude squared inside and near one period of the nanostructure shown in Fig. 24 with monochromatic illumination.

5. Personnel Supported

Y. Fainman, PI, Professor

P. C. Sun, Assistant Research Scientist

Paul Shames, Research Assistant

Rong Tyan, Research Assistant

James Thomas, Research Assistant

Wataru Nakagawa, Research Assistant

Lijun Zhu, Research Assistant

Guy Klemens, Research Assistant

Sandra Chien, Research Assistant

Chia Ho Tsai, Research Assistant